Characterization of the Microstructure, Crystallographic Texture and Segregation of an As-cast Duplex Stainless Steel Slab

Clara Herrera, Dirk Ponge, Dierk Raabe

Max-Planck-Institut für Eisenforschung GmbH, Max-Planck-Str. 1, 40237 Düsseldorf, Germany; d.ponge@mpie.de

The microstructure of a duplex stainless steel slab 1.4362 produced by continuous casting has been investigated by optical microscopy, scanning electron microscopy, EBSD and EDS. The slab showed different macrostructures through the thickness. The macrostructure can be divided into 3 types: fine equiaxed, columnar and coarse equiaxed grains. In all three regions, the volume fraction of each phase austenite and delta-ferrite is close to 50% and the hardness is very similar for both. The austenite has Kurdjumov-Sachs or Nishiyama-Wassermann relationship with the delta-ferrite. The slab does not show a strong segregation profile through the thickness. The delta-ferrite is enriched in Cr and Mo, while austenite is enriched in Ni and Mn.

Keywords: duplex stainless steel, as-cast slab, microstructure, texture, EBSD, segregation

DOI: 10.2374/SRI08SP014-79-2008-482; submitted on 10 December 2007, accepted on 20 February

Introduction

Duplex stainless steels (DSSs) are based on the Fe-Cr-Ni system and consist of ferrite (30-70%) and austenite. DSSs have shown an excellent combination of resistance to general and localized corrosion, stress corrosion cracking, high strength and low cost due to reduced contents of Ni and Mo [1-3]. DSSs are used in oil, gas, paper, desalination and petrochemical industries.

The main process steps in the industrial manufacturing of duplex stainless steel sheets are continuous casting, slab reheating, hot rolling, coiling, hot band heat treatment, cold rolling and final recrystallization annealing. Particular attention during manufacturing of these steels has to be paid to the forming steps at high temperatures. Hot working of steels with two phases may cause complications for several reasons: the precipitation of detrimental phases [1,4], such as σ-phase and $M_{23}C_6$, the low hot ductility, and edge crack formation. The ductility depends on different factors like temperature, strain rate, microstructure and chemical composition. Moreover, it is affected by the different softening mechanisms in ferrite and austenite [5-9].

The formation of as-cast microstructures of duplex stainless steels depends on undercooling, cooling rates and subsequent solid state transformations which are influenced by the local chemical composition [1,10-12]. Duplex stainless steels solidify by forming primary ferrite with austenite precipitates either from the liquid or in the solid state during cooling. The amount of austenite and its morphology depend on the cooling rate. At increased cooling rate the amount of austenite is reduced [10-14].

The austenite can have a specific orientation relationship with the ferrite matrix. Grains that have been formed by a α-γ phase transformation should show a Bain, Nishiyama-Wassermann (N-W), or Kurdjumov-Sachs (K-S) orientation relationship. These orientation relationships can be described as a rotation of an angle ω about a common crystallographic axis (axis of rotation), this angle and axis are known as angle/axis pair, **Table 1**.

Owing to these aspects associated with the microstructural state of the two phases prior to hot working the present study investigates in detail the microstructure, the crystallographic microtexture, and the segregation of an as-cast duplex stainless steel slab produced by continuous casting (duplex stainless steel 1.4362).

Table 1. Orientation relationship between austenite (γ) and ferrite matrix (α).

Orientation relationship	Lattice correspondence relation	Misorientation angle/axis
Bain	{001}γ // {001}α <110>γ // <110>α	45° / <001>
Kurdjumov-Sachs (K-S)	{111}γ // {011}α <011>γ // <111>α	42.8° / <2 2 11>
Nishiyama-Wassermann (N-W)	{111}γ // {011}α <112>γ // <011>α	45.9° / <254>

Table 2. Chemical composition of the 1.4362 duplex stainless steel (mass %).

C	Si	Mn	Cr	Mo	Ni	Ti	Nb	Cu
0.024	0.220	1.39	22.32	0.14	3.65	0.012	0.010	0.410

Experimental

The duplex stainless steel slab of 240mm thickness was produced by continuous casting under standard industrial condition. The chemical composition of the slab is given in **Table 2**.

Microstructural observations, optical and scanning electron microscopy (SEM) were performed on the plane normal to the transverse direction after standard sample preparation and etching using the solutions Beraha I [15] or V2A-etchant [16]. The volume fraction of the phases was quantified by optical microscopy and ferritoscope measurement (Helmut Fischer GmbH, model Feritscope

MP30E). No significant differences between the obtained values from both methods were found in this study.

A chemical analysis was performed by an energy dispersion spectroscopy (EDS) device attached to the SEM. Orientation imaging microscopy of the microstructure by automated EBSD measurements was applied. The step size for the measurements was between 1 and 10µm. Microhardness measurements were conducted using a load of 0.5 N.

Results and Discussion

Figure 1 shows the solidification macrostructure of the slab. The macrostructure of the slab consists of three zones: (a) a fine equiaxed zone at the top and bottom (Regions 1 and 4), (b) a columnar zone under the fine equiaxed zone on the top (Region 2), and (c) the equiaxed zone in the centre of the slab (Region 3). The macrostructure through the thickness of the slab is heterogeneous.

Figure 2 shows a calculated portion of the phase diagram of the duplex stainless steel. After solidification and slow cooling, a coarse two-phase structure is observed. The as-cast microstructure is characterized by a ferrite matrix with austenite precipitates on the grain boundaries or inside the grains. **Figure 3 to 5** show the microstructure and **Table 3** the volume fraction of ferrite in the different zones of the slab. The slab does not reveal a strong gradient of the volume fraction of the two phases through the thickness. The ferrite solidifies first. The austenite precipitates in the solid state. The precipitation of austenite occurs by a nucleation and growth process. The austenite morphology can be characterized by Dubé [17] and Aaronson's [18] morphological classification scheme.

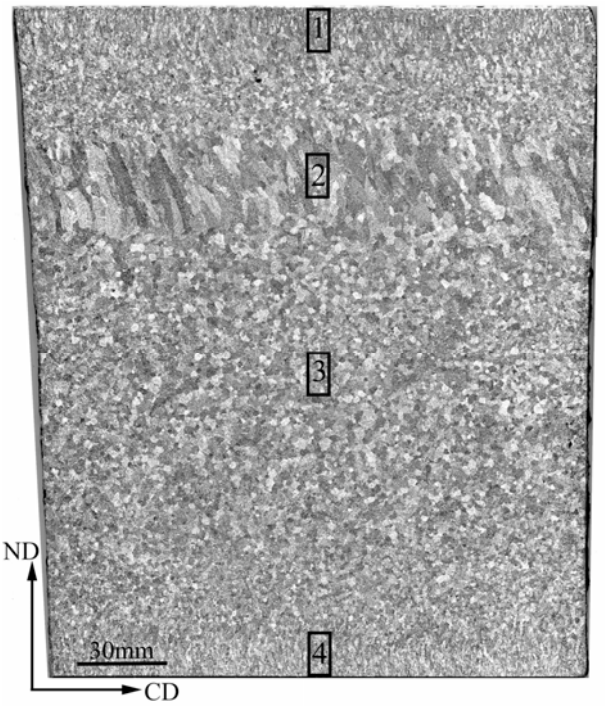

Figure 1. Macrostructure of duplex stainless steel 1.4362.

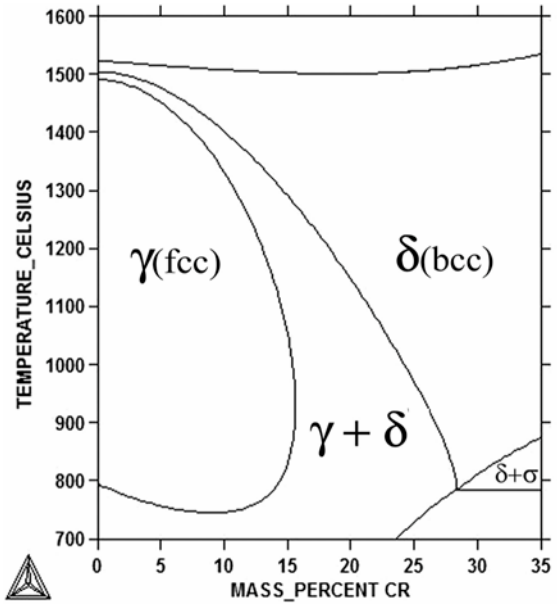

Figure 2. Cross-section of calculated phase diagram of Fe-Cr-3%Ni-0.14%Mo-1.4%Mn alloy.

Table 3. Volume fraction of ferrite in the different regions of the slab (cf. Figure 1).

Region	% Ferrite
1	49.3 ± 3.4
2	52.1 ± 3.9
3	56.2 ± 4.5
4	48.1 ± 3.9

Table 4. Hardness of austenite and ferrite in the four regions.

Region	Hardness, HV	
	Austenite	Ferrite
1	284.4 ± 11.6	284.8 ± 11.8
2	270.8 ± 13.8	280.8 ± 11.4
3	275.1 ± 17.2	255.3 ± 6.7
4	291.1 ± 13.9	281.7 ± 10.5

The austenite shows grain boundary allotriomorphs, Widmanstätten needles, or continuous films morphologies, respectively.

In the fine equiaxed zones (regions 1 and 4), the solidification is faster than in the other zones; therefore, the micostructure is finer. Austenite allotriomorphs are formed first at the ferrite grain boundaries. Starting from them Widmanstätten austenite needles extend inside the ferrite grains. Large arrays of parallel austenite needles are observed.

Region 2 exhibits columnar ferrite grains with continuous austenite films on the grain boundaries. Long austenite needles or bigger allotriomorphs can also be detected.

In the centre of the slab, region 3, the ferrite shows equiaxial grains which are larger than the ferritic grains at the top and bottom of it due to the slow cooling rate.

The hardness of the austenite and ferrite do not change substantially through the thickness (**Table 4**). The hardness

values are common duplex stainless steels [19-21]. The ferrite in the middle of the slab shows a low hardness due to the coarse grain size in this region.

The slab does not show substantial segregation through the thickness. The concentration of Cr, Ni, Mn and Mo in the austenite and ferrite are very similar in the four regions. **Figure 6** shows the distribution of Fe, Cr, Ni, Mn in both phases as a function of the partition coefficient K_i.

Distribution maps of Cr, Ni, Mn, Si and Mo were collected together with the corresponding EBSD scans (**Figure 7c** and **7d**). The EBSD technique is sensitive to different lattice parameters as well as to crystallographic orientations.

In the regions 1 and 4, the distribution of the elements is homogeneous. In regions 2 and 3, Mn and Si show a homogeneous distribution in both phases while ferrite is Cr-enriched and austenite is Ni-enriched. This elemental partitioning corresponds to the stabilizing effect of each element [22-25]. The distribution of Mo is homogeneous between both phases in regions 1, 3 and 4 but it is not detectable in region 2 because the concentration of Mo is too low for a quantitative measurement by EDS. Ohmori et al. [22] reported that the partition of Mo between austenite and ferrite was very minor compared with Ni and Cr partitions.

The decomposition of δ-ferrite can take place by the nucleation and growth process with partitioning of Ni and Cr atoms between the austenite and the ferrite [26]. The partition must occur at the ferrite-austenite grain boundary during cooling. The variation of the elemental distribution in the different regions is related to the cooling rate. It is fastest in regions 1 and 4. Consequently, the time for diffusion processes is shorter compared with the other zones. In the regions 2 and 3, the slow cooling favours the diffusion of the elements.

The texture of the slab is not strong but it shows a gradient through the thickness. **Figure 8** shows pole figures for austenite and ferrite determined by EBSD. In region 2, the ferrite texture is strongest. Regions 1 and 4 show the weakest texture. The ferrite texture in regions 2 and 3 is more pronounced due to the slower cooling rate. The austenite texture shows a weak intensity in all regions compared with the ferrite texture. The ferrite texture develops during the solidification process, while the austenite texture results from the $\delta \rightarrow \gamma$ transformation.

In regions 1 and 4, the ferrite grains forms {001}<110> and {012}<321> components. The austenite phase shows a strong component close to {110}<332> and a weak {001}<021> component. In region 2, the texture of the ferrite is characterized by {001}<210> and {112}<021> and the austenite by {110}<113> and {001}<120> texture components. The ferrite texture is tilted, approximately 10°, in relation to the normal direction due to the thermal gradient. In region 3, the ferrite shows a texture fibre <001>//ND and austenite shows {110}<113> and {032}<123> components.

During continuous casting, the top and bottom of the slab solidified at first with a high cooling rate. The ferrite

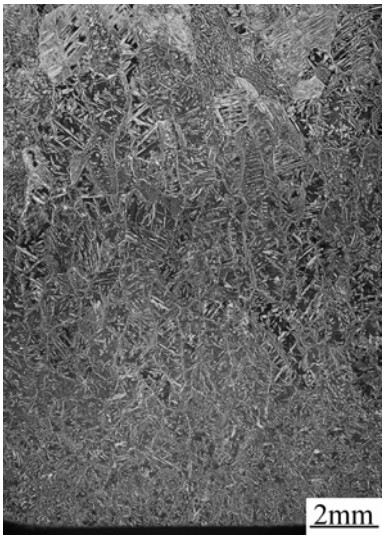

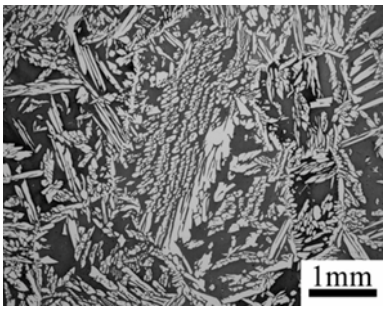

Figure 3. Microstructure at the top and the bottom of the slab, region 1.

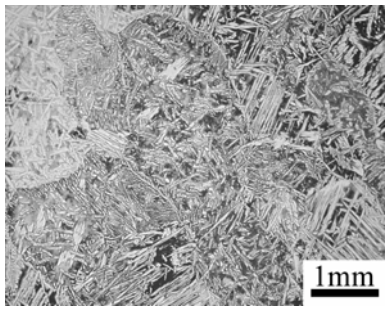

Figure 4. Microstructure of the columnar zone, region 2.

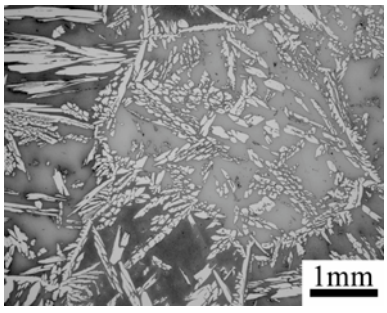

Figure 5. Microstructure at the middle of the slab, region 3.

texture in these regions is almost random due to the heterogeneous nucleation at the interface between the mould walls and the liquid metal in the solidification, as known from other conventional casting processes. In region 2, the columnar ferrite grains are elongated in the direction of the heat flow, and have a strong crystallographic texture. In region 3, equiaxed grains are formed with a more random texture compared with the columnar region [27].

A favourable orientation in the solidification process occurs when the direction of growth is perpendicular to the mould wall, for cubic metals, the preferred growth direction is <001>, which results in the gradual strengthening of the <001>//ND fibre texture. The ferrite texture of the slab is a typical texture observed in the solidification of cubic metals. The solidification texture of the ferrite is in principal comparable to earlier observations on single phase α- and γ- stainless steels [28-30].

Figures 7a and **7b** show a phase map with the orientation relationships between δ and γ obtained by EBSD measurements of one of the samples, region 2. **Figure 9** shows the distribution of the misorientation angle between δ and γ boundaries. The used tolerances for the orientation relationship are 2.5° or 5° around the misorientation angle. The misorientation of the three regions lies in the interval of 40-50°, which contains both the Nishiyama-Wassermann (N-W) and the Kurdjumov-Sachs (K-S) crystallographic orientation relationships. The Bain orientation relationship is not observed in any of the three regions. The misorientation angle distribution for this interval reveals a maximum around 44° ± 2°. The phase map (**Figure 7b**) shows that the austenite precipitates with a near N-W or K-S orientation relationship with at least one grain. This result agrees with earlier results from the literature [31,32]. The distribution of the orientation relationships shows that the K-S orientation relationship occurs more frequently than the N-W orientation relationship. It also shows that the variant 1 of the K-S orientation relationship [33], $(111)\gamma//(011)\alpha$ - $[\bar{1}01]\gamma//[1\,\bar{1}\,1]\alpha$, is the most frequent one. This behaviour was found in all three regions. Most of the Widmanstätten needles and allotriomorphs of the austenite grow with a specific orientation relationship with the ferrite and do so close to K-S or N-W relationships.

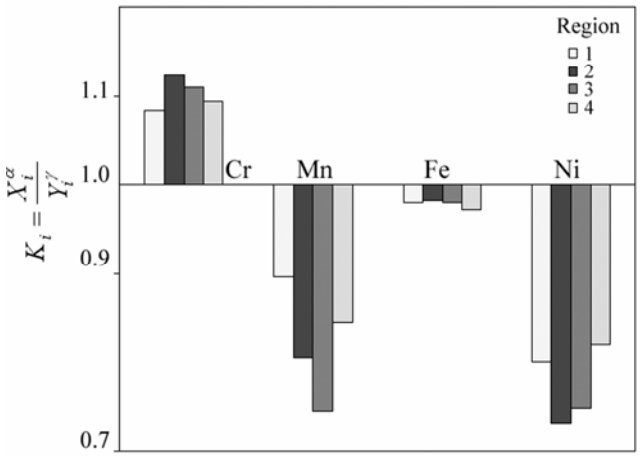

Figure 6. Partition coefficient of the alloying elements in the three regions.

The austenite regions, which grow by a reconstructive mechanism into the ferrite grains, tend to grow without a strict crystallographic orientation relationship into only one

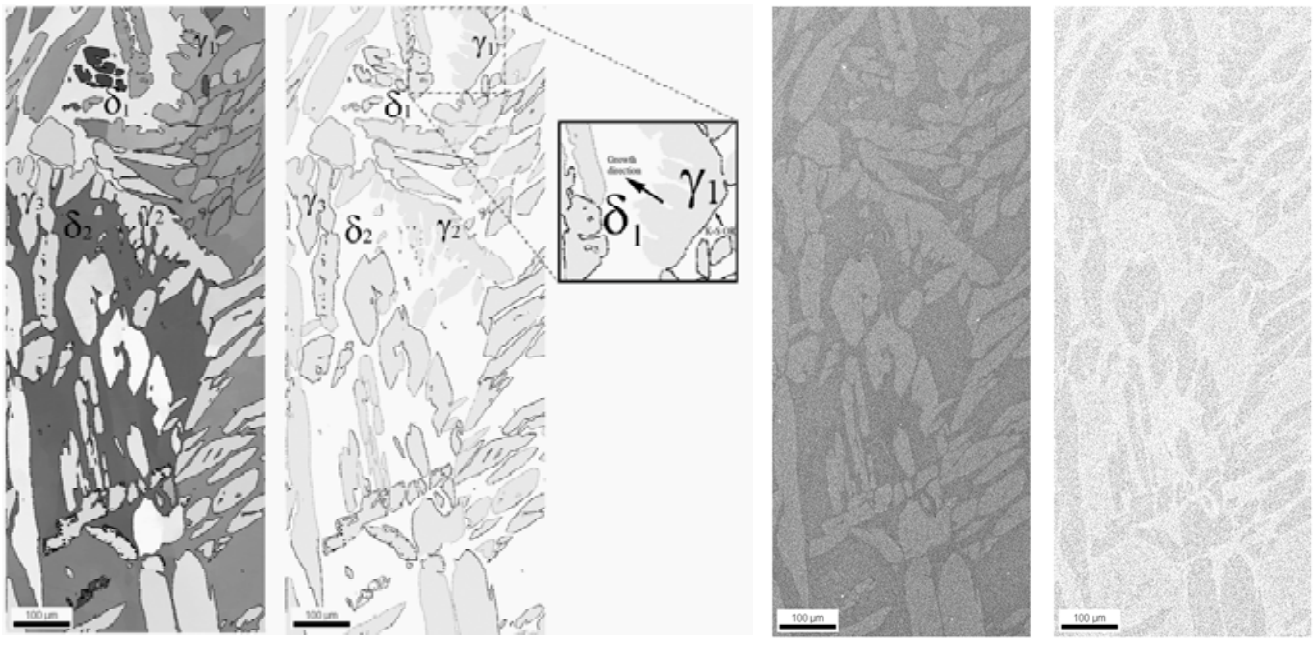

Figure 7. EBSD orientation map of the region 2: (a) IPF map showing the orientation of the two phases; (b) grain average misorientation map between δ ferrite (white) and austenite (grey); (b) EDS map of Cr distribution and (c) EDS map of Ni distribution.

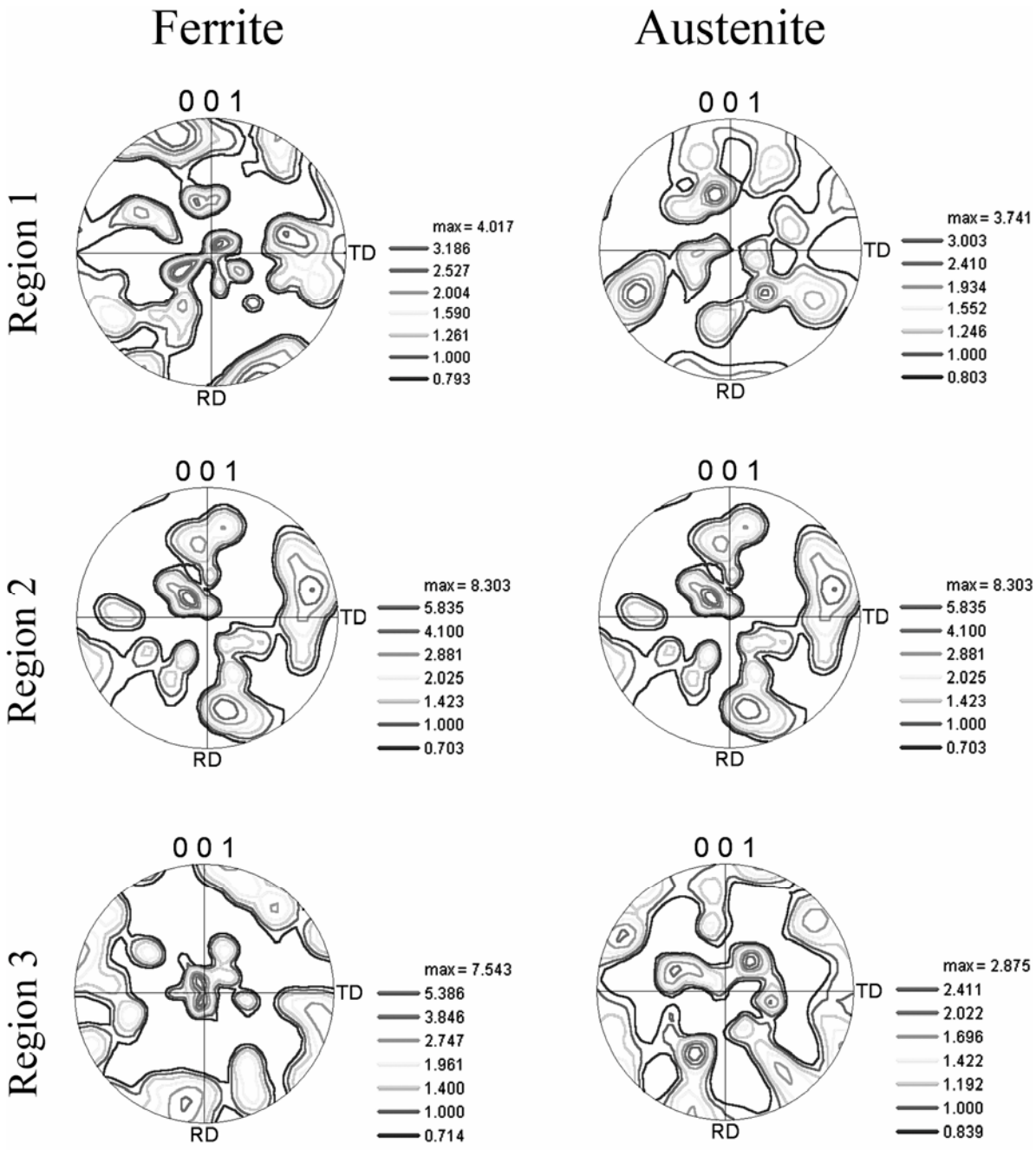

Figure 8. {001} Pole figures of austenite and δ ferrite of the three regions.

δ-ferrite grain. The other side of the γ grain, which nucleates with a low-energy grain boundary, does not move and has a preferred orientation relationship [31,32,34,35]. Austenitic grains, which are identified as γ_1 and γ_2, grow into δ_1 and δ_2, respectively, this behaviour is shown in **Figure 7b**. In some cases, austenite grows into both δ grains with a specific orientation relationship, e.g. γ_3 grows into δ_1 and δ_2 (**Figure 7b**).

The δ-ferrite solidifies preferentially in the [100] direction and the austenite precipitates holding a specific relationship with their ferrite matrix. Davies et al. [36] observed that the phase transformation in a commercial duplex α - β brass (59.5%Cu-40.5%Zn) is also orientation dependent. The measurement of the α-brass texture that these authors conducted in their work was characterized by a cube texture, {001}<100>, a texture fibre running from the {110}<112> to the near {112}<111> orientation, and a further fibre texture between {103}<010> and {101}<010>. This texture is similar to the texture that would be predicted using the K-S relationship between β- and α-brass.

The α-brass textures from this earlier work and the γ textures observed in the current study are comparable. Therefore, it is concluded that the δ-γ transformation can be described by the K-S or N-W type relationships. Finally, when the cooling of the continuous casting is slow, the transformation takes place close to thermal equilibrium and any crystallographic relationship in a diffusive solid-state transformation can develop more accurate [37].

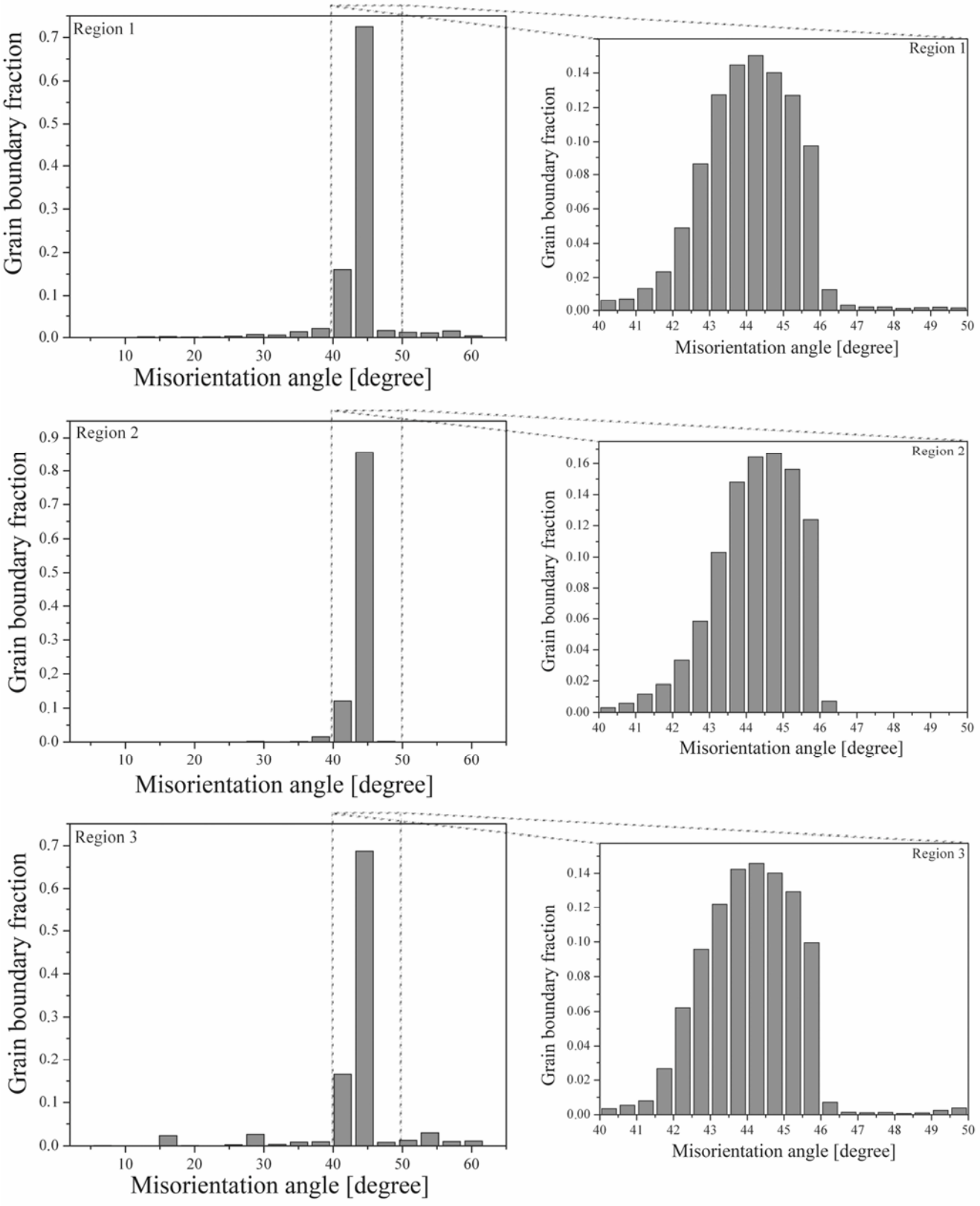

Figure 9. Histograms of misorientation angle distribution between δ ferrite and austenite of the three regions.

Conclusions

The duplex stainless steel slab produced by continuous casting showed a ferritic-austenitic microstructure. The austenite precipitated at the grain boundaries or inside the δ-ferrite with Nishiyama-Wassermann (N-W), or Kurdjumov-Sachs (K-S) orientation relationship to the ferrite. The phase fractions were constant through the thickness. After solidification, an equal volume fraction of ferrite and austenite, close to 50-50%, was obtained for the

temperature range between 1200 to 1100°C. The cooling rate from this temperature range to room temperature was similar everywhere in the slab. Consequently, the volume fraction of the phases did not show a significant variation through the thickness. The austenite morphology can be described by Dubé and Aaronson's morphological classification. The slab shows a finer microstructure at the top and bottom, a small columnar region close to the top and a coarse equiaxed microstructure in the middle. The ferrite texture is a typical solidification texture, dominated by <100>//ND, and it is strongest in the columnar region. The austenite texture is weaker. The element partitioning between δ ferrite and austenite is stronger in the columnar and equiaxed regions near the centre of the slab due to the slower cooling rate favouring diffusion. In these regions, austenite is enriched in Ni and Mn while δ ferrite has more Cr and Mo.

References

[1] J.-O. Nilsson: Materials Science Technology, 8 (1992), No. 8, 685-700.

[2] H.D. Solomon, T.M. Devine: Duplex Stainless Steel - A tale of two phase, Conference Duplex Stainless Steel'82, 1982 St. Louis, USA, Proceedings. Metals Park, Ohio, ASM, 1983, p.693-756.

[3] D. Noble: Selection of wrought duplex stainless steel, ASM Handbook, Metals Park, Ohio; ASM International, 6 (1993), p.471-781.

[4] A. Wilson, J.-O. Nilsson: Scand. J. Metallurgy, 25 (1996), No. 4, 178-185.

[5] E. Evangelista, H.J. McQueen, M. Niewczas, M. Cabibbo: Canadian Metall. Quarterly, 43 (2004), No. 3, 339-354.

[6] O. Balancin, W.A.M. Hoffmann, J.J. Jonas: Metall. Mat. Trans. A, 31 (2000), No. 5, 1353-1364.

[7] L. Duprez, B.C. De Cooman, N. Akdut: Steel Research, 73 (2002), No. 12, 531-538.

[8] A. Iza-Mendia, A. Pinol-Juez, J.J. Urcola, I. Gutierrez: Metall. Mat. Trans. A, 29 (1998), No. 12, 2975-2986.

[9] J.M. Cabrera, A. Mateo, L. Llanes, J.M. Prado, M. Anglada: J. Materials Processing Technology, 143-144 (2003), p. 321-325.

[10] Z.M. Cvijovic, D.V. Mihajlovic, V.R. Knezevic: Materials Science Forum, 282-283 (1998), 323-330.

[11] E. Gariboldi, N. Lecis, F. Bonollo, N. Gramegna, W Nicodemi: Advanced Engineering Materials, 4 (2002), No. 1-2, 33-37.

[12] C. Herrera, N.B. de Lima, A.M. Kliauga and A.F. Padilha: Materials Characterization, 59 (2008), No. 1, 79-83.

[13] E. Johnson, L. Gråbæk, A. Johansen, L. Sarholt Kristensen: Materials Science Engineering, 98 (1988), 301-303.

[14] S.A David, J.M. Viteck, T.L. Hebble: Welding Research Sup., (1987), No. 10, p. 289S-300S.

[15] E. Weck, E. Leistner: Metallographische Anleitung zum Farbätzen nach dem Tauchverfahren, Teil II, Deutscher Verlag für Schweisstechnik, München, Germany, 1983.

[16] G. Petzow: Metallographisches Ätzen, Gebrüder Bornträger, Berlin, Germany, 1984.

[17] C. Dubé, H. Aaronson, R.F. Mehl: Revue de Metallurgie, 55 (1958), No. 3, 201-210.

[18] H. Aaronson, in: Decomposition of austenite by diffusional processes, ed. V. Zachay, H. Aaronson, Interscience Publishers, 1962, pp. 387-546.

[19] A. Ulhaq, H. Weiland, H.J. Bunge: Materials Science and Technology, 10 (1994), No. 4, 289-298.

[20] A.F. Padilha, V. Randle, I.F. Machado: Materials Science and Technology, 15 (1999), No.9, 1015-1018.

[21] M. Martins, L.C. Casteletti: Materials Characterization, 55 (2005), 225-233.

[22] Y. Ohmori, K. Nakai, H. Ohtsubo, Y. Isshiki. ISIJ International, 35 (1995), No. 8, 969-975.

[23] S. Atamert, J.E. King: Acta Metall. Mat., 39 (1991), No.3, 273-285.

[24] T.H. Chen, J.R. Yang: Materials Science Eng A, 311 (2001), 28-41.

[25] J.M. Vitek, S.A. Vitek, S.A. David. Metallurgical and Materials Transactions A, 26 (1995), No. 8, 1995-2007.

[26] P.D. Southwick and R.W.K Honeycombe: Metal Science, 14 (1980), No. 7, 253-261.

[27] B. Chalmers: Principles of solidification, John Wiley & Sons, Inc., New York, 1967.

[28] D. Raabe: Metallurgical Materials Transactions A, 26 (1995), No. 4, 991-998.

[29] D. Raabe: Materials Science and Technology, 11 (1995), No. 5, 461-468.

[30] D. Raabe: Acta Materialia, 45 (1997), No. 3, 1137-1151

[31] K. Ameyama, G.C. Weatherly, K.T. Aust: Acta Metall. Mater., 40 (1992), No. 8, 1835-1846.

[32] E.F. Monlevade, I.G.S. Falleiros: Metallurgical Materials Transaction A, 37 (2006), No. 3, 939-949.

[33] S. Morito, H. Tanaka, R. Konishi, T. Furuhara, T. Maki: Acta Materialia, 51 (2003), 1789-1799.

[34] C.H. Shek, C. Dong, J.K.L. Lai, K.W. Wong: Metallurgical Materials Transactions A , 31 (2000), No. 1, 15-19.

[35] H. Landheer, S.E. Offerman, R.H. Petrov, L.A.I Kestens, Materials Science Forum, 558-559 (2007), 1413-1418.

[36] G.J. Davies, J.S. Kallend, P.P. Morris: Acta Metallurgical, 24 (1976), 159-172.

[37] H.J. Bunge, W. Weiss, H. Klein, L. Wcislak, U. Garbed, J. R. Schneider: J. Applied Crystallography, 36 (2003), 137-140.